Chemical Science

ROYAL SOCIETY OF CHEMISTRY

EDGE ARTICLE

View Article Online
View Journal | View Issue

Cite this: *Chem. Sci.*, 2025, **16**, 12096

All publication charges for this article have been paid for by the Royal Society of Chemistry

Received 21st April 2025
Accepted 27th May 2025

DOI: 10.1039/d5sc02884a

rsc.li/chemical-science

Interstitial nitrogen modified Rh nanocrystals for efficient and CO-resistant alkaline hydrogen oxidation electrocatalysis†

Jianchao Yue, Chaoyi Yang, Yu Zhang, Qianqian Xiong and Wei Luo *

The preparation of active and CO-tolerant platinum-free electrocatalysts toward the hydrogen oxidation reaction (HOR) under alkaline conditions is significant for the practical development of anion exchange membrane fuel cells. Herein, nitrogen atoms are intercalated into the interstitial void of rhodium (N–Rh/C) nanocrystals, which results in electron-deficient and electron-rich Rh sites simultaneously to coordinate the binding energies of multiple key intermediates, achieving highly active and CO-resistant alkaline HOR. *In situ* surface-enhanced infrared absorption spectroscopy and density functional theory calculations illustrate that the introduction of interstitial N atoms suppresses the electronic back-donation from Rh 4d to the CO 2π* orbital in electron-deficient sites, thereby weakening the CO adsorption and improving CO resistance. Additionally, the enhanced OH adsorption in electron-rich sites can release more free water into the adjacent gap region, increasing water connectivity and hydrogen-bond networks in the electrical double layer and accelerating alkaline HOR kinetics.

Introduction

Hydrogen fuel cells have garnered considerable attention in addressing the pressing issues of energy crises and environmental pollution.[1–3] The advancement of non-noble metal-based catalysts in alkaline environments significantly mitigates the reliance on precious metals in the cathodic oxygen reduction reaction (ORR), positioning anion exchange membrane fuel cells (AEMFCs) as ideal devices.[4–7] However, the kinetics under alkaline conditions has decreased by several orders of magnitude compared to acidic conditions for the hydrogen oxidation reaction (HOR), which has observably hindered the large-scale application of AEMFCs.[8,9] Furthermore, hydrogen produced by current industrial methods inevitably contains a certain amount of CO, and purification will lead to a substantial increase in costs.[10–12] The reason for the poisoning and deactivation of active sites caused by CO adsorption is the strong electronic back-donation behavior from metal d to the CO 2π* orbitals.[13] Therefore, current research focuses on weakening the chemical CO adsorption by modulating the electronic structure of the catalyst.[14–18] However, it remains challenging to prepare alkaline HOR catalysts that simultaneously satisfy high activity and CO tolerance.

At present, the d-band center theory is mainly relied upon to describe the binding strength between various intermediates and the catalyst surface, and its downward shift is considered to reflect the weakening of intermediate adsorption.[19,20] However, for electrocatalytic processes involving multiple reactants, single-type electronic regulation of the catalyst is far from sufficient. For instance, the downward shift of the metal d-band center will reduce the binding energy of H and CO, which is conducive to alkaline HOR, but will lead to an attenuated OH binding energy concurrently.[21,22] It has been reported that enhancing the hydroxyl binding energy (OHBE) can promote the oxidation of surface-adsorbed H and CO and accelerate the HOR process.[23,24] Besides, Chen and his colleagues proposed that the hydrogen-bond network in the electrical double layer (EDL) during alkaline hydrogen electrode reactions becomes sparse (*i.e.*, there is a gap region) due to the presence of bulky cations, while OH adsorption can increase the H_2O_{gap} content, enhance the connectivity of the water network, and thereby promote the transport of H^+.[25] However, adjusting the metal active sites purposefully according to the adsorption requirements of different intermediates to achieve simultaneous optimization of binding strength is indispensable but also challenging for constructing excellent alkaline HOR catalysts.

Unlike traditional alloying and doping, interstitial alloying can change the electronic structure of metals without affecting the surface reaction of the catalyst and can make full use of active sites.[26–29] Herein, we have successfully constructed interstitial N modified Rh supported on carbon (N–Rh/C) through colloidal synthesis and hydrothermal methods. DFT calculation results show that when the N atoms are inserted into the interstitial sites of Rh nanocrystals, the CO*/H* adsorption sites become electron-deficient while the OH* adsorption sites

College of Chemistry and Molecular Sciences, Wuhan University, Wuhan, Hubei 430072, P. R. China. E-mail: wluo@whu.edu.cn

† Electronic supplementary information (ESI) available. See DOI: https://doi.org/10.1039/d5sc02884a

become electron-rich, thus simultaneously optimizing the adsorption of multiple intermediates. *In situ* surface-enhanced infrared absorption spectroscopy (SEIRAS) indicates that N–Rh/C suppresses the electronic back-donation from Rh 4d to the CO $2\pi^*$ orbital, thereby weakening the CO adsorption. Moreover, enhanced OH adsorption promotes the transformation of the interfacial water type, increasing the water content in the gap region and improving the connectivity of the interfacial water network within the EDL. Consequently, N–Rh/C exhibits excellent alkaline HOR catalytic activity and CO tolerance, with a mass activity is 8.0 times higher than that of Rh/C and 2.7 times higher than that of Pt/C, respectively.

Results and discussion

The synthesis schematic diagram illustrates the general synthetic process for N–Rh/C in Fig. 1a, where Rh nanoparticles were obtained by colloidal synthesis and then small N atoms were inserted into them by hydrothermal methods. Powder X-ray diffraction (XRD) analyses in Fig. 1b were conducted to confirm that the crystal structures of the catalysts are matched well to the standard Rh (PDF# 87-0714). The (111) peak at 41° shows a slight negative shift about 0.3°, indicating lattice expansion due to the introduction of N atoms into the interstitial sites of the Rh crystal structure. The valence state and chemical composition of the catalyst surface were characterized by X-ray photoelectron spectroscopy (XPS). Fig. 1c depicts the high-resolution Rh 3d spectra of N–Rh/C, which can be separated into metallic peaks (Rh^0 $3d_{3/2}$, 312.1 eV; Rh^0 $3d_{5/2}$, 307.4 eV) and oxidized Rh species (Rh^{3+} $3d_{3/2}$, 313.1 eV; Rh^{3+} $3d_{5/2}$, 308.4 eV).[30,31] Compared with Rh/C, the Rh^0 peaks exhibit 0.3 eV positive shift, indicating the electron transport from Rh to N, which resulted in the electron-deficient state of Rh atoms. The N 1s XPS spectra (Fig. 1d) show two peaks at 397.9 and 399.9 eV, corresponding to the N–Rh bond and pyrrolic N.[32,33] The atomic proportion of Rh and N in N–Rh/C is 16.58% and 2.97%, respectively, according to the XPS results shown in Table S1.† The transmission electron microscopy (TEM) images show uniformly dispersed nanoparticles and the average size is about 2.81 nm as shown in Fig. 1e. Combining the similar morphology and particle size of Rh/C (Fig. S1†), the difference in activities caused by particle size is eliminated. The high-resolution STEM images prove that the lattice spacing in the (200) plane of N–Rh nanoparticles is 0.195 nm, and the lattice spacing in the (111) plane is 0.229 nm, which are slightly expanded compared with 0.190 nm and 0.219 nm in conventional Rh, confirming the successful introduction of N at the interstitial position of Rh

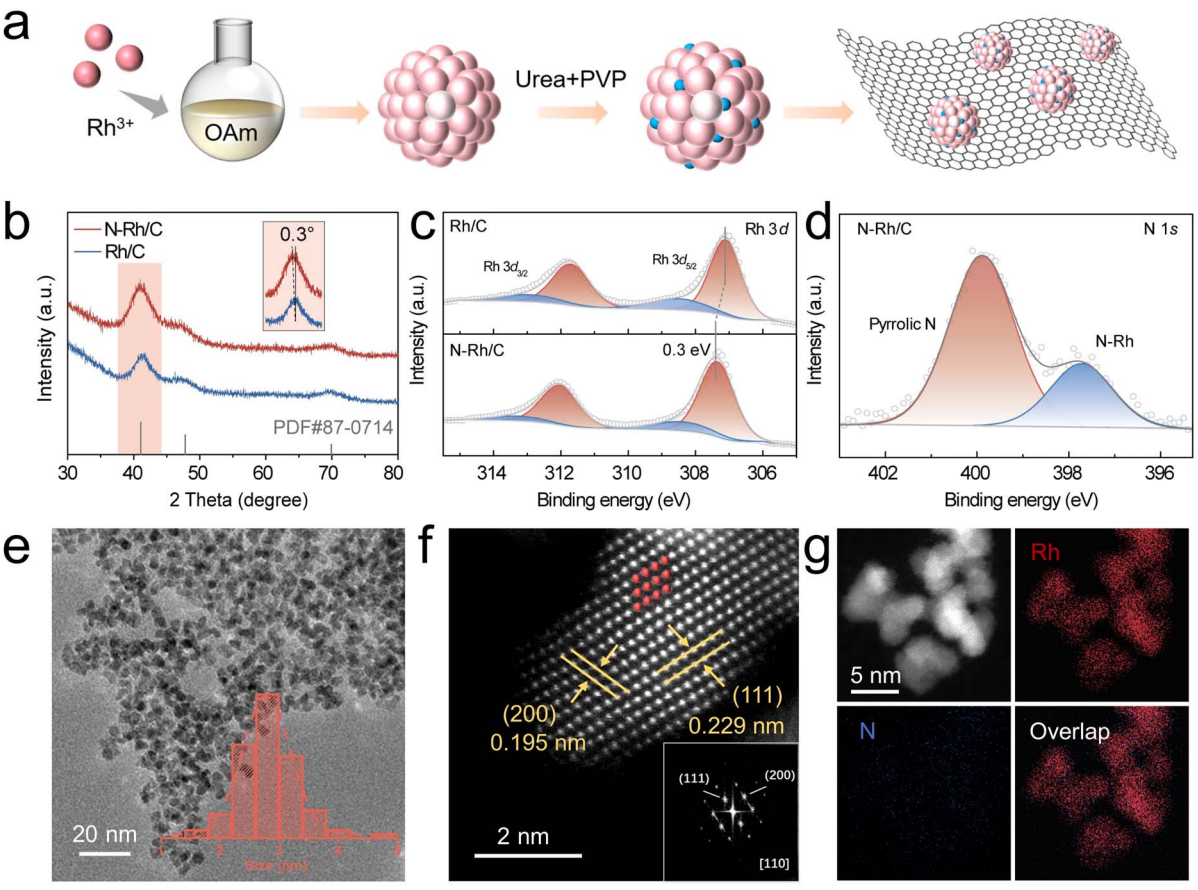

Fig. 1 (a) The synthesis process diagram for N–Rh/C. (b) XRD patterns of N–Rh/C and Rh/C. (c) The Rh 3d XPS spectra of N–Rh and Rh/C. (d) XPS spectra of N 1s in N–Rh. (e) TEM image of N–Rh. The inset shows the average size of the particles. (f) HAADF-STEM image of the N–Rh. The inset shows the corresponding FFT diffraction pattern of N–Rh. (g) HAADF-STEM elemental mapping of the N–Rh with Rh (red), N (blue), and overlap.

nanoparticles. The corresponding fast Fourier transform (FFT) pattern further confirms this (Fig. 1f).[34] Furthermore, the elemental distribution of the N–Rh nanoparticles was studied using HAADF-STEM energy-dispersive X-ray (EDX) mapping (Fig. 1g), in which the Rh and N are uniformly distributed. The line-scan electron energy loss spectroscopy (EELS) spectra were collected for the N–Rh nanoparticle (Fig. S2†), showing distinct Rh M_3-edge and N K-edge signals.

X-ray absorption structure (XAS) spectroscopy measurements were performed to ascertain the local coordination environment of N–Rh/C. Fig. 2a shows the normalized Rh K-edge XANES spectra of N–Rh/C. With Rh foil and Rh_2O_3 as reference, the line of N–Rh/C displayed a positive shift, and the average valence of Rh in N–Rh/C is determined to be +1.1, which means that Rh transfers electrons outward (Fig. 2b).[35] The extended X-ray absorption fine structure (EXAFS) spectra of N–Rh/C show the local coordination environment around Rh sites as shown in Fig. 2c, in which the peak at 1.5 Å belongs to the Rh–O/N bond, and the peak at 2.4 Å indicates the Rh–Rh bond. The quantitative least squares EXAFS fitting analysis obtained the local chelation parameters around the Rh sites, and the corresponding fitted structural parameters are shown in Fig. 2d and listed in Table S2.† Two different local coordination structures of Rh–Rh coordination shell and Rh–O/N coordination shell for N–Rh/C with the average bond lengths of 2.45 and 1.56 Å, which show coordination numbers of 7.9 and 2.7, reveal that N atoms are inserted into the lattice gap of Rh successfully. The wavelet-transform (WT) corresponding to the Rh K-edge EXAFS (Fig. 2e–g) further verified the Rh–Rh and Rh–N bonds in N–Rh/C, further confirming the nitridation of Rh nanoparticles.

The electrocatalytic performance toward alkaline HOR of the obtained samples was evaluated with a standard three-electrode system in an H_2-saturated 0.1 M KOH electrolyte. As shown in Fig. 3a, the current density of N–Rh/C shows a significant enhancement compared with Rh/C and commercial Pt/C, manifesting the significance of interstitial nitrogen in improving the HOR activities. According to the simplified Butler–Volmer equation (Fig. S3†), the micro-polarization region (−5 to 5 mV) further confirms the improvement of performance. The influence of N-doping amount on the catalyst activity is studied by changing the input amount of urea. As shown in Fig. S4,† N–Rh/C with an input amount of 240 mg urea has the best performance. Furthermore, in order to exclude the influence of H_2 mass transport and obtain kinetic current densities (j^k), the HOR polarization curves of N–Rh/C as a function of the rotation rate at rotation speeds from 625 to 2500 rpm were investigated to obtain the relevant kinetic parameters (Fig. S5†), for which the increased plateau current density along with the elevated rotation rate indicates accelerated mass transport. The corresponding Koutecky–Levich plot was constructed, in which the j^{-1} exhibits a linear relationship with the $\omega^{-1/2}$ (Fig. S5–S7†).[36] The kinetic current densities (j^k) of the HOR on the N–Rh/C, Rh/C, and Pt/C electrodes were extracted using the Koutecky–Levich equation. The corresponding Tafel plots of the samples are presented in Fig. 3b.[37–39] Based on the inductively coupled plasma atomic emission spectroscopy (ICP-AES) results in Table S3,† the normalized mass activity denoted as $j^{k,m}$ at the overpotential of 50 mV of the N–Rh/C is 1.04 mA μg_{Rh}^{-1}, which is 8.0 and 2.7 times greater than those of the Rh/C (0.13 mA μg_{Rh}^{-1}) and Pt/C (0.38 mA μg_{Pt}^{-1}), respectively. Furthermore, N–Rh/C also presents the highest $j^{0,m}$ among the tested samples (Fig. S8†). The electrochemically active surface areas (ECSAs) was tested by the Cu underpotential deposition (Cu_{upd}) to investigate the intrinsic activities of different catalysts (Fig. S9†). The ECSA normalized exchange current density ($j^{0,s}$) was estimated. As shown in Fig. 3c, N–Rh/C unambiguously exhibited the highest $j^{0,s}$ of 0.73 mA cm^{-2}, which is approximately three times higher than those

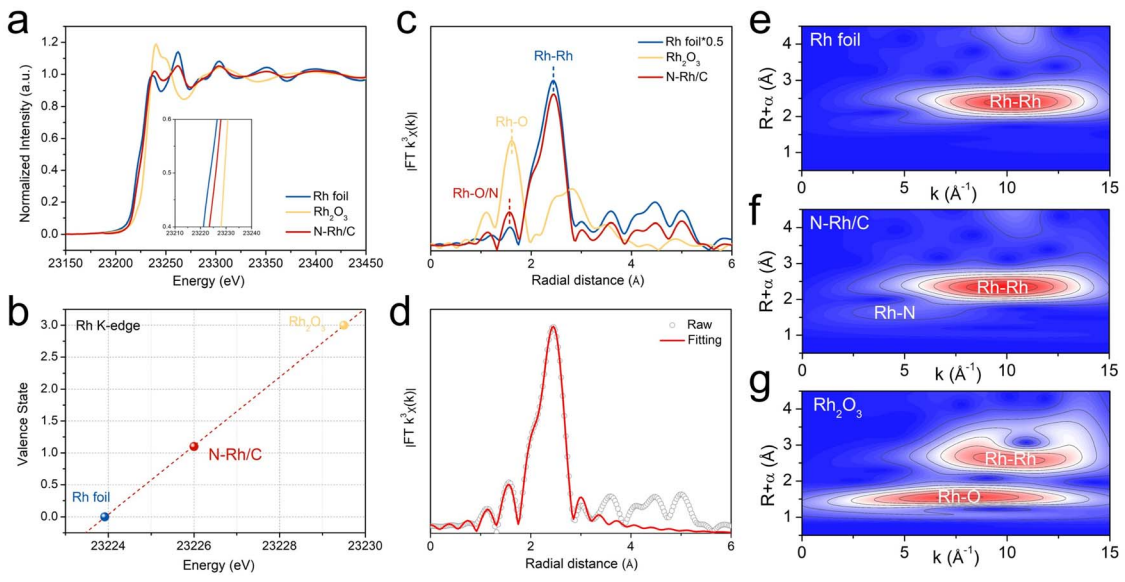

Fig. 2 (a) Rh K-edge XANES spectra of N–Rh/C in reference to Rh foil and Rh_2O_3. (b) Determination of Rh oxidation in N–Rh/C. (c) Fourier transform of EXAFS spectra for Rh. (d) EXAFS fitting curves in the *R* space of N–Rh/C. Wavelet transforms for the k^3-weighted Rh K-edge EXAFS of Rh foil (e), N–Rh/C (f) and Rh_2O_3 (g).

of Rh/C (0.27 mA cm^{-2}) and Pt/C (0.23 mA cm^{-2}). Furthermore, the exchange current density of N–Rh/C outperforms most of the platinum-group metal (PGM)-based HOR catalysts in the previous reports (Fig. S10 and Table S4†).

In recent years, with continuous exploration and discoveries by previous studies regarding the pH effect involved in the hydrogen oxidation reaction (HOR), it has been found that some catalysts exhibit inflection point behavior, that is, the apparent activity (j^0) initially decreases and then increases as the pH of the electrolyte increases. This phenomenon not only challenges the traditional belief that higher alkalinity leads to slower HOR kinetics but also highlights the intensity of hydroxyl adsorption as a primary descriptor for HOR activity under alkaline conditions.[40,41] Therefore, further investigation into the activity optimization mechanism of N–Rh/C was conducted by measuring pH-universal HOR polarization curves (Fig. S11 and Table S5†). As shown in Fig. 3d, at pH ~7, the j^0 of N–Rh/C abnormally increases. The same situation occurs at Rh/C, but it shows an abnormally increased j^0 only at pH ~8.2 as shown in Fig. S12.† Moreover, CO stripping experiments indicated that the peak of CO oxidation for the N–Rh/C catalyst shifted negatively by 35 mV compared to that of Rh/C (Fig. 3e), suggesting a stronger binding affinity between N–Rh/C and OH*.[42] The zeta potential experiments manifest the strengthened OHBE as well, on the basis of more negative charge of N–Rh/C (−25.76 mV) than Rh/C (−15.16 mV) as shown in Fig. S13.† The stability tests of the catalysts were carried out by conducting 1000 cyclic voltammetry (CV) measurements to test the stability of the catalyst. The polarization curve and CV curve (Fig. S14†) of N–Rh/C did not attenuate significantly before and after the stability test, and the exchange current density was maintained at 97.16%, which was better than that of Rh/C (Fig. S15†), highlighting the excellent stability of N–Rh/C. In addition, the structure of the catalyst remains basically unchanged after the stability test (Fig. S16†). The N 1s XPS spectra after the stability test also show the existence of the interstitial N as shown in Fig. S17.†

Limited by the means of hydrogen production, the hydrogen used at the anode side will inevitably contain trace CO impurities. The CO adsorbed on the catalyst active site competes with the intermediates H* and OH* involved in the HOR process, causing catalyst poisoning and resulting in reduced activity and even catalyst inactivation.[17,43] The CO resistance for the catalysts was evaluated by the HOR polarization curves before and after a chronoamperometry test under 1000 ppm CO/H_2. Compared with the initial curve without CO poisoning, in the first cycle curve after CO poisoning, the current density of N–Rh/C retained 50.8% at 0.05 V, while that of Rh/C only retained 5.14%

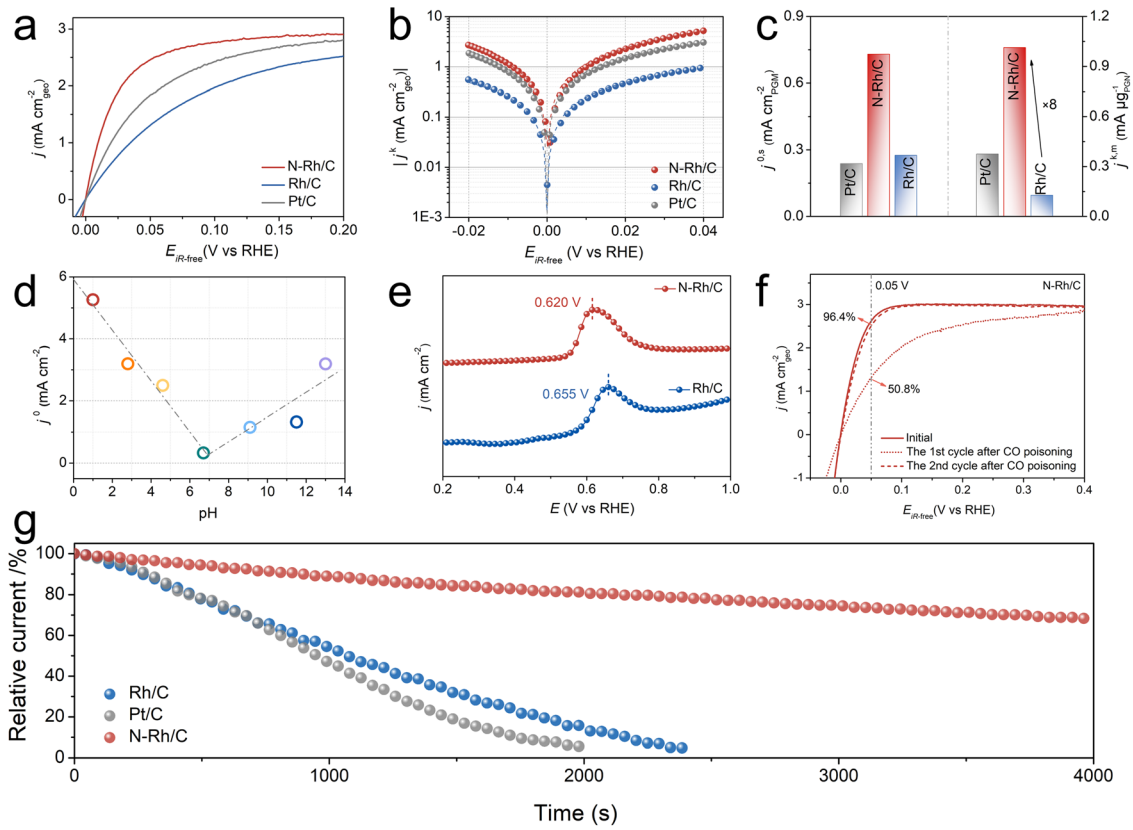

Fig. 3 (a) HOR polarization curves of N–Rh/C, Rh/C, and Pt/C in H_2-saturated 0.1 M KOH. (b) Tafel plots derived from (a), normalized j^k by the Butler–Volmer fittings. (c) Comparison of the mass activities ($j^{k,m}$) at 50 mV and the ECSA-normalized exchange current densities ($j^{0,s}$) of N–Rh/C, Rh/C, and Pt/C. (d) Non-monotonous relation between j^0 and the pH of N–Rh/C. (e) CO stripping curves of N–Rh/C and Rh/C. (f) HOR polarization curves before (solid line) and after (dashed line) the chronoamperometry test of N–Rh/C in H_2-saturated 0.1 M KOH solution. (g) I–t curves obtained at 0.1 V *vs.* RHE in 1000 ppm CO/H_2-saturated 0.1 M KOH solution.

(Fig. 3f and S18†), which indicates that the surface of N–Rh/C absorbed less CO and the adsorption capacity was weaker. As the electric potential increases, the adsorbed CO may oxidize/desorb with the adsorbed OH, resulting in reversible recovery of the poisoned active site.[44] As expected, in the second cycle curve at 0.05 V, the current density of N–Rh/C can recover to 96.4%, while that of Rh/C only recovers to 53.3%. Based on the above experimental phenomena, it can be reasonably inferred that N–Rh/C has weaker CO adsorption capacity, and the enhanced OH adsorption releases the toxic active site, thus achieving excellent CO resistance. *I–t* curves in Fig. 3g are obtained by chronoamperometry tests at 0.1 V *vs.* RHE in 1000 ppm CO/H_2-saturated 0.1 M KOH solution. The current density of Rh/C and commercial Pt/C rapidly deactivates in 2000 s, while N–Rh/C can still retain 70% at 4000 s, indicating the superior CO tolerance (Table S6†).

Many studies have shown that CO adsorption is related to the transfer of electrons from metal 4d to the CO 2π* orbital.[45] In general, the more electrons are transferred in reverse, the stronger the Rh–C bonds and the weaker the corresponding C–O bonds. Therefore, *in situ* SEIRAS can be used to determine the extent of electron back-donation and its effect on CO adsorption.[46,47] As shown in Fig. 4a and S19,† SEIRAS spectra of N–Rh/C and Rh/C were collected at the potential from 0 to 0.8 V in a CO-saturated 0.1 M KOH solution, and the peaks of ~2100 cm^{-1} could be attributed to the CO adsorbed on the Au film substrate. The CO adsorption on the catalyst is divided into two types due to its different state: bridge adsorption ($*CO_B$) at around 1850 cm^{-1} and linear adsorption ($*CO_L$) at around 1950 cm^{-1}, among which the adsorption of $*CO_L$ is the main cause of catalyst poisoning. First, compared with Rh/C, the peak strength of both $*CO_B$ and $*CO_L$ in N–Rh/C is significantly reduced, indicating lower CO coverage on its surface, which indirectly reflects its weak CO adsorption. In addition, the blueshift of peaks occurs with incremental potentials, which is consistent with the decrease of back-donation from the Rh 4d to the CO 2π* orbitals, leading to the weakened CO adsorption. A function between the CO vibrational wavenumber and the applied potential was constructed as shown in Fig. 4b and S20.† At the same potential, the absorption peak frequency of N–Rh/C is higher than that of Rh/C, indicating that its CO adsorption is weakened. Moreover, the higher stark tuning rates of $*CO_B$ (105 *vs.* 101 cm^{-1} V^{-1}) (Fig. S16†) and $*CO_L$ (135 *vs.* 85 cm^{-1} V^{-1}) (Fig. 4b) for N–Rh/C indicate the decrease of CO coverage, which further proves that the CO adsorption is inhibited and explains the strong tolerance of N–Rh/C to CO.

The interfacial water structure in the electrical double layer (EDL) on the catalyst surface can also be observed by *in situ* SEIRAS.[48,49] The O–H stretching vibration peak (2800–3800 cm^{-1}) of interfacial water can be deconvoluted into three different types of water, namely, the water molecule located in the gap region (H_2O_{gap}, ~3600 cm^{-1}), the water molecule located above the interstitial region ($H_2O_{above\text{-}gap}$, ~3400 cm^{-1}) and the water molecule near the electrode surface ($K{\cdot}H_2O$, ~3200 cm^{-1}), in which the H_2O_{gap} can be used as an index to judge the connectivity of the hydrogen-bond network (H-bond network) (Fig. 4c and S21†).[25,50,51] Compared with Rh/C, N–Rh/C has a higher proportion of H_2O_{gap} and it improves with the increase of the applied potential (Fig. 4d). Upon analyzing the proportional changes of various types of interfacial water as

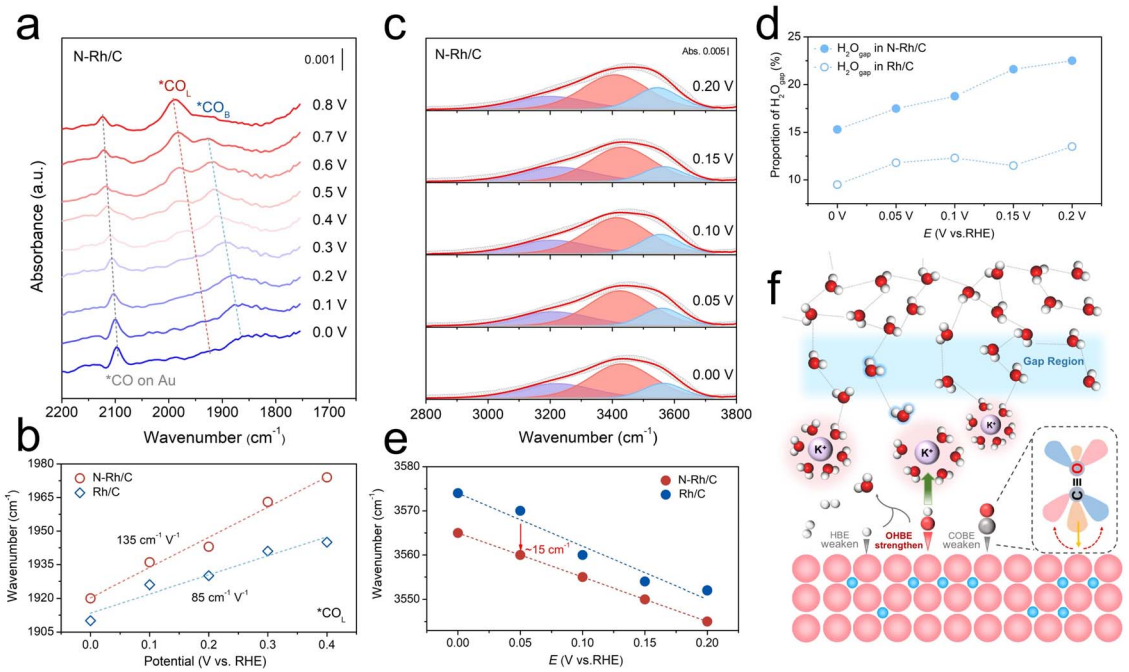

Fig. 4 (a) *In situ* SEIRAS depicting the CO adsorption state of the N–Rh/C. (b) Linear-bound CO on N–Rh/C as a function of potential. (c) Deconvolution of the O–H stretching vibration features of *in situ* SEIRAS spectra. (d) Proportion of H_2O_{gap} from *in situ* SEIRAS spectra. (e) Comparison of the O–H stretching vibration frequencies of H_2O_{gap} of N–Rh/C and Rh/C from *in situ* SEIRAS spectra. (f) Schematic illustration of alkaline HOR and CO resistance.

shown in Fig. S22,† it was found that as the potential increased, the proportion of $K{\cdot}H_2O$ decreased, and the proportion of H_2O_{gap} increased, while that of $H_2O_{above\text{-}gap}$ remained largely stable. Therefore, the enhanced OH adsorption on N–Rh/C can prompt more OH species to coordinate with K^+, causing them to release more free water into the adjacent gap region to construct H-bond network. Moreover, the O–H stretching bond of H_2O_{gap} moves ~15 cm^{-1} toward the lower wavenumber (Fig. 4e), indicating that the increased concentration of water in the gap region, which can further promote the H-bond network continuity. This further leads to abnormal behavior of the catalyst's activity under lower pH conditions – an earlier appearance of the inflection point. These phenomena represent that N–Rh/C has a better proton transport and improves the reaction kinetics of alkaline HOR. Consequently, the function of interstitial N atoms achieves the enhancement of CO resistance and HOR activity by weakening CO adsorption but strengthening OHBE (Fig. 4f).

Density functional theory (DFT) calculations were carried out to gain an in-depth understanding of the structure–adsorption relationship. First, in order to prove that N atoms are more inclined to intercalate into the Rh octahedral interspace than to replace the Rh atoms, the corresponding structural model is calculated as shown in Fig. 5a. The intercalation behavior has lower formation energy, indicating that its structure is more stable. This verifies the rationality of the N–Rh structure prepared in this work and provides a basis for the subsequent DFT calculation.[32,33] As shown in Fig. S23,† Rh (111) and N–Rh (111) models are constructed. According to the calculated charge density difference on Rh (111) before and after the introduction of interstitial N, as shown in Fig. S24,† it can be determined that there is an obvious electronic interaction between the interstitial N and the surrounding Rh sites. The adsorption energy of H* and OH* and the key intermediates involved in the alkaline HOR process were calculated following the structural models shown in Fig. S25 and S26.† N–Rh exhibits a Gibbs free energy for H* (ΔG_{H^*}) of −0.206 eV, indicating weaker hydrogen binding strength compared to Rh (−0.254 eV) (Fig. 5b), which is consistent with the hydrogen underpotential deposition (H_{upd}) findings from cyclic voltammetry (CV) experiments (Fig. S27†).[52,53] The lower binding strength facilitates the rapid adsorption or desorption of H intermediates during the reaction, promoting their binding with other intermediates. The Gibbs free energy for OH* (ΔG_{OH^*}) on N–Rh (0.333 eV) was significantly enhanced than that of Rh (0.472 eV) in Fig. 5b, which is conducive to the oxidation of H* and CO*.[17,43] Moreover, the enhancement of OHBE can promote the connectivity of the hydrogen bond network in the EDL and promote the reaction kinetics, which is the reason why the alkaline HOR activity of N–Rh/C is increased.[50,51] In addition, compared with Rh, the adsorption energy of CO* on N–Rh is reduced (Fig. S28 and S29†), which is consistent with the *in situ* SEIRAS results (Fig. 4a). Combined with the computational model and previous studies, CO* and H* compete for the same active site, so the adsorption strength of the two on the catalyst surface was compared. As shown in Fig. 5c, the introduction of N atoms significantly reduced the

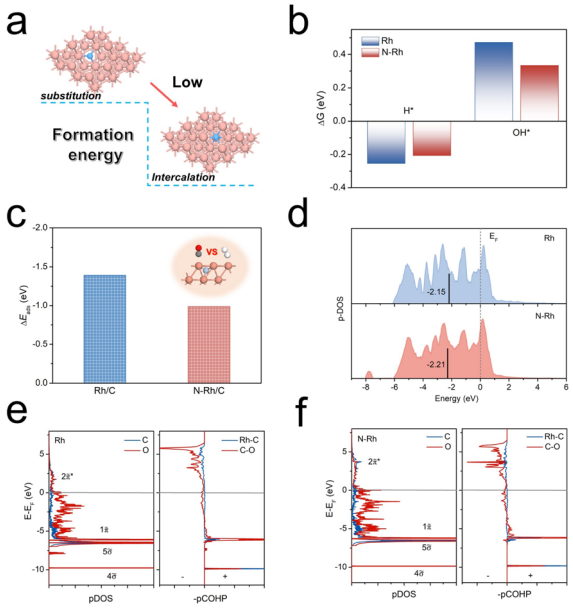

Fig. 5 (a) The top view calculation models of N doped Rh in substituting Rh atom and intercalating into the Rh octahedral interspace. Rh and N atoms are denoted by pink and blue spheres. (b) Gibbs free energy schematic plot for the adsorption of H* and OH* on the surface of Rh and N–Rh. (c) The adsorption energy difference ΔE_{ads} ($E_{ads,CO} - E_{ads,H2}$) of Rh and N–Rh. (d) The pDOS of Rh 4d orbitals in Rh and N–Rh. The pDOS and −pCOHP curves for CO adsorption on (e) Rh and (f) N–Rh surfaces.

difference in adsorption energy between CO* and H*, improved the adsorption competitiveness of H*, and thus promoted the CO-resistant ability of the catalyst. The projected partial density of states (pDOS), in Fig. 5d, shows the position of the d-band center (E_d) of N–Rh further away from the Fermi level (E_f), weakening the H* adsorption and reducing the degree of the electron back-donation from Rh 4d to CO 2π*.[54,55] In order to further explore the reason for the attenuated COBE/HBE but enhanced OHBE, by analyzing the computational models, it is found that CO*/H* tends to be adsorbed at the same site and OH* at another site (Fig. S25, S26 and S28†). According to the calculated charge density difference on Rh (111) before and after the introduction of interstitial N, the influence of interstitial N on the Rh site is nonhomogeneous. As shown in Fig. S30,† the electron deficiency state around the CO*/H* site reduces the degree of the electron back-donation from Rh 4d to CO 2π* and shows the position of the d-band center (E_d) of N–Rh further away from the Fermi level (E_f), weakening the CO adsorption, while electron accumulation around the OH* site led to the opposite adsorption result.[56,57] The Bader charge analysis also indicates that the CO*/H* sites tend to lose electrons and the OH* sites tend to gain electrons.

By tracking the molecular orbital interactions between CO adsorbents and Rh active sites in different models, the reasons for inhibiting CO adsorption were explored in depth. Specifically, CO internal bonds and Rh–CO interactions on catalysts were revealed by C- and O-projected density of states (pDOS) and projected crystal orbital Hamilton population (pCOHP) (Fig. 5e and f). Compared with Rh, the 2π̃* orbital of CO on the

N–Rh surface is at a higher energy level and less occupied, indicating weaker CO adsorption and activation. In addition, the reduction of the occupied bond orbitals of Rh–C on N–Rh relative to Rh can be quantitatively obtained by integrating the projected crystal orbital Hamilton population (IpCOHP) (Table S7†), which also confirms the reduction of CO adsorption.[58–60] The results of orbital analysis show that the filling of interstitial N atoms at the octahedral site of Rh can reduce the chemisorption of CO by inhibiting the electron back-donation from the Rh 4d to the CO 2π* orbitals. Based on all the studies conducted, the interstitial N atoms have the capability to modulate the electronic structure of the Rh sites, leading to an augmentation of OHBE and a decrease in both HBE and COBE (CO binding energy). These alterations collectively contribute to the enhancement of alkaline HOR activity and the promotion of CO tolerance.

Conclusions

In summary, we demonstrated that interstitial N modified N–Rh/C nanoparticles can be used as a highly efficient and CO-resistant catalyst for alkaline HOR, with the mass activity being 8.0 and 2.7 times higher than those of Rh/C and commercial Pt/C. Density functional theory calculations manifest that the existence of interstitial N leads to an electron-losing state at the CO*/H* site, which causes the upshifted d-band center to weaken HBE and suppress electronic back-donation from Rh 4d to the CO 2π* orbital, and an electron-gaining state at the OH* site, thus optimizing the binding energies of multiple intermediates simultaneously. Meanwhile, the observed inflection point behavior reflects the importance of hydroxyl adsorption, and according to *in situ* SEIRAS, the optimization of hydrogen-bond network continuity caused by OHBE enhancement also confirmed the acceleration of HOR kinetics. This work not only provides a unique direction for the design of advanced metal-based catalysts, but will also inspire the exploration of efficient catalysts for multi-intermediate reactions.

Data availability

The data supporting this article have been included as part of the ESI.†

Author contributions

JY, CY, YZ and QX performed the material synthesis and electrochemical tests. JY performed the DFT calculations. WL supervised the work. JY and WL wrote the manuscript.

Conflicts of interest

There are no conflicts to declare.

Acknowledgements

This work was financially supported by the National Natural Science Foundation of China (22272121 and 21972107) and National Key Research and Development program of China (2021YFB4001200). The numerical calculations in this paper have been done on the supercomputing system in the supercomputing center of Wuhan University. We thank the team at the BL11B beamline in the Shanghai Synchrotron Radiation Facility (SSRF) for the XAFS measurements. We thank the team at the Core Facility of Wuhan University for the ICP-AES and XPS measurements. We also thank the team at the Core Research Facilities of College of Chemistry and Molecular Sciences, and the Center for Electron Microscopy at Wuhan University for their substantial support of TEM measurements.

Notes and references

1 L. Schlapbach and A. Züttel, *Nature*, 2001, **414**, 353–358.
2 B. P. Setzler, Z. Zhuang, J. A. Wittkopf and Y. Yan, *Nat. Nanotechnol.*, 2016, **11**, 1020–1025.
3 C. Gunathilake, I. Soliman, D. Panthi, P. Tandler, O. Fatani, N. A. Ghulamullah, D. Marasinghe, M. Farhath, T. Madhujith, K. Conrad, Y. Du and M. Jaroniec, *Chem. Soc. Rev.*, 2024, **53**, 10900–10969.
4 H. A. Gasteiger and N. M. Markovic, *Science*, 2009, **324**, 48–49.
5 N. Ramaswamy and S. Mukerjee, *Chem. Rev.*, 2019, **119**, 11945–11979.
6 X. Wu, N. Chen, H. A. Klok, Y. M. Lee and X. Hu, *Angew. Chem., Int. Ed.*, 2021, **61**, e202114892.
7 Y. Gao, Y. Yang, R. Schimmenti, E. Murray, H. Peng, Y. Wang, C. Ge, W. Jiang, G. Wang, F. J. DiSalvo, D. A. Muller, M. Mavrikakis, L. Xiao, H. D. Abruña and L. Zhuang, *Proc. Natl. Acad. Sci. U. S. A.*, 2022, **119**, e2119883119.
8 S. Zhu, X. Qin, F. Xiao, S. Yang, Y. Xu, Z. Tan, J. Li, J. Yan, Q. Chen, M. Chen and M. Shao, *Nat. Catal.*, 2021, **4**, 711.
9 C. Yang, Z. Dai, J. Yue, G. Wang and W. Luo, *Chem. Sci.*, 2025, **16**, 5266–5274.
10 T. Wang, L.-Y. Li, L.-N. Chen, T. Sheng, L. Chen, Y.-C. Wang, P. Zhang, Y.-H. Hong, J. Ye, W.-F. Lin, Q. Zhang, P. Zhang, G. Fu, N. Tian, S.-G. Sun and Z.-Y. Zhou, *J. Am. Chem. Soc.*, 2022, **144**, 9292–9301.
11 R. Chaubey, S. Sahu, O. O. James and S. Maity, *Renewable Sustainable Energy Rev.*, 2013, **23**, 443–462.
12 G. Huang, Y. Wu, Y. Li, S. Du, Q. Liu, M. Li, D. Zhang, Z. Jiang, S. Zhong, S. Lu, L. Tao and S. Wang, *Adv. Funct. Mater.*, 2025, **35**, 241535.
13 H.-R. Pan, T. Tang, Z. Jiang, L. Ding, C. Xu and J.-S. Hu, *J. Phys. Chem. Lett.*, 2024, **15**, 3011–3022.
14 F. Gao, S. Liu, J. Ge, X. Zhang, L. Zhu, Y. Zheng, Y. Duan, S. Qin, W. Dong, X. Yu, R. Bao, P. Yang, Z. Niu, Z. Ding, W. Liu, S. Lan, M. Gao, Y. Yan and S. Yu, *Nat. Catal.*, 2022, **5**, 993–1005.
15 B. Zhang, B. Zhang, G. Zhao, J. Wang, D. Liu, Y. Chen, L. Xia, M. Gao, Y. Liu, W. Sun and H. Pan, *Nat. Commun.*, 2022, **13**, 5894.
16 X. Wang, Y. Tong, W. Feng, P. Liu, X. Li, Y. Cui, T. Cai, L. Zhao, Q. Xue, Z. Yan, X. Yuan and W. Xing, *Nat. Commun.*, 2023, **14**, 3767.

17 Y. Zhou, Z. Xie, J. Jiang, J. Wang, X. Song, Q. He, W. Ding and Z. Wei, *Nat. Catal.*, 2020, **3**, 454–462.
18 P. Wang, Y. Yang, W. Zheng, Z. Cheng, C. Wang, S. Chen, D. Wang, J. Yang, H. Shi, P. Meng, P. Wang, H. Tong, J. Chen and Q. Chen, *J. Am. Chem. Soc.*, 2023, **145**, 27867–27876.
19 Y. K. Feng, S. G. Lu, L. H. Fu, F. L. Yang and L. G. Feng, *Chem. Sci.*, 2024, **15**, 2123–2132.
20 N. Acerbi, S. C. E. Tsang, G. Jones, S. Golunski and P. Collier, *Angew. Chem., Int. Ed.*, 2013, **52**, 7737–7741.
21 T. He, W. Wang, F. Shi, X. Yang, X. Li, J. Wu, Y. Yin and M. Jin, *Nature*, 2021, **598**, 76–81.
22 Z. Xia and S. Guo, *Chem. Soc. Rev.*, 2019, **48**, 3265–3278.
23 L. Wei, N. Fang, F. Xue, S. Liu, W.-H. Huang, C.-W. Pao, Z. Hu, Y. Xu, H. Geng and X. Huang, *Chem. Sci.*, 2024, **15**, 3928–3935.
24 F. Yang, X. Bao, P. Li, X. Wang, G. Cheng, S. Chen and W. Luo, *Angew. Chem., Int. Ed.*, 2019, **58**, 14179–14183.
25 P. Li, Y. Jiang, Y. Hu, Y. Men, Y. Liu, W. Cai and S. Chen, *Nat. Catal.*, 2022, **5**, 900–911.
26 Y. Li, C.-K. Peng, H. Hu, S.-Y. Chen, J.-H. Choi, Y.-G. Lin and J.-M. Lee, *Nat. Commun.*, 2022, **13**, 1143.
27 T. Chen, I. Ellis, T. J. N. Hooper, E. Liberti, L. Ye, B. T. W. Lo, C. O'Leary, A. A. Sheader, G. T. Martinez, L. Jones, P.-L. Ho, P. Zhao, J. Cookson, P. T. Bishop, P. Chater, J. V. Hanna, P. Nellist and S. C. E. Tsang, *J. Am. Chem. Soc.*, 2019, **141**, 19616–19624.
28 R. Guo, Q. Chen, X. Li, Y. Liu, C. Wang, W. Bi, C. Zhao, Y. Guo and M. Jin, *J. Mater. Chem. A*, 2019, **7**, 4714–4720.
29 T. Chen, C. Foo and S. C. Edman Tsang, *Chem. Sci.*, 2021, **12**, 517–532.
30 Y. Zhang, G. Li, Z. Zhao, L. Han, Y. Feng, S. Liu, B. Xu, H. Liao, G. Lu, H. L. Xin and X. Huang, *Adv. Mater.*, 2021, **33**, 2105049.
31 H. Huang, K. Liu, F. Yang, J. Cai, S. Wang, W. Chen, Q. Wang, L. Fu, Z. Xie and S. Xie, *Angew. Chem., Int. Ed.*, 2023, **62**, e202315752.
32 M. Xie, B. Zhang, Z. Jin, P. Li and G. Yu, *ACS Nano*, 2022, **16**, 13715.
33 Y. Zheng, B. Zhang, T. Ma, R. Yan, W. Geng, Z. Zeng, Y. Zhang and S. Li, *Small*, 2023, **20**, 2307405.
34 Y. Guo, X. Yang, X. Liu, X. Tong and N. Yang, *Adv. Funct. Mater.*, 2022, **33**, 2209134.
35 J. Hu, X. Wang, H. Liu, H. Li, Yi. Zhou, M. Liu, C. Wang, M. Li, Y. Tang and G. Fu, *Chem. Sci.*, 2025, **16**, 1837–1848.
36 L. Wang, Z. Xu, C. H. Kuo, J. Peng, F. Hu, L. Li, H. Y. Chen, J. Wang and S. Peng, *Angew. Chem., Int. Ed.*, 2023, **62**, e202311937.
37 S. Wang, L. Fu, H. Huang, M. Fu, J. Cai, Z. Lyu, Q. Wang, Q. Kuang, Z. Xie and S. Xie, *Adv. Funct. Mater.*, 2023, **33**, 2304125.
38 H. Shi, Y. Yang, P. Meng, J. Yang, W. Zheng, P. Wang, Y. Zhang, X. Chen, Z. Cheng, C. Zong, D. Wang and Q. Chen, *J. Am. Chem. Soc.*, 2024, **146**, 16619–16629.
39 Z. Huang, R. Lu, Y. Zhang, W. Chen, G. Chen, C. Ma, Z. Wang, Y. Han and W. Huang, *Adv. Funct. Mater.*, 2023, **33**, 2306333.
40 Y. Jin, X. Fan, W. Cheng, Y. Zhou, L. Xiao and W. Luo, *Angew. Chem., Int. Ed.*, 2024, **63**, e202406888.
41 P. Han, X. Yang, L. Wu, H. Jia, J. Chen, W. Shi, G. Cheng and W. Luo, *Adv. Mater.*, 2024, **36**, 2304496.
42 J. Fang, H. Wang, Q. Dang, H. Wang, X. Wang, J. Pei, Z. Xu, C. Chen, W. Zhu, H. Li, Y. Yan and Z. Zhuang, *Nat. Commun.*, 2024, **15**, 4236.
43 Y. C. Hou, T. Shen, K. Hu, X. Wang, Q. N. Zheng, J. B. Le, J. C. Dong and J. F. Li, *Angew. Chem., Int. Ed.*, 2024, **63**, e202402496.
44 C. Yang, G. Wang, J. Yue, Z. Dai and W. Luo, *ACS Catal.*, 2024, **15**, 869–876.
45 B. Cai, X. Chen, L. Wang and H. Fu, *ACS Catal.*, 2024, **14**, 13602–13629.
46 Y. Dong, Z. Zhang, W. Yan, X. Hu, C. Zhan, Y. Xu and X. Huang, *Angew. Chem., Int. Ed.*, 2023, **62**, e202311722.
47 C. Jin, Y. Liao, A. Zhang, S. Zhao, R. Wang, J. Li and H. Tang, *Nano Energy*, 2024, **122**, 109305.
48 Q. Sun, N. J. Oliveira, S. Kwon, S. Tyukhtenko, J. J. Guo, N. Myrthil, S. A. Lopez, I. Kendrick, S. Mukerjee, L. Ma, S. N. Ehrlich, J. Li, W. A. Goddard, Y. Yan and Q. Jia, *Nat. Energy*, 2023, **8**, 859–869.
49 K. Zhao, X. Chang, H. S. Su, Y. Nie, Q. Lu and B. Xu, *Angew. Chem., Int. Ed.*, 2022, **61**, e202207197.
50 Y. H. Wang, Y. Yang, F. Y. Gao, X. L. Zhang, L. Zhu, H. K. Yan, P. P. Yang and M. R. Gao, *Angew. Chem., Int. Ed.*, 2024, **63**, e202407613.
51 J. Yue, Y. Li, C. Yang and W. Luo, *Angew. Chem., Int. Ed.*, 2024, **64**, e202415447.
52 M. Ma, G. Li, W. Yan, Z. Wu, Z. Zheng, X. Zhang, Q. Wang, G. Du, D. Liu, Z. Xie, Q. Kuang and L. Zheng, *Adv. Funct. Mater.*, 2022, **12**, 2103336.
53 J. Zheng, W. Sheng, Z. Zhuang, B. Xu and Y. Yan, *Sci. Adv.*, 2016, **2**, e1501602.
54 M.-W. Gu, H. H. Peng, I. W. P. Chen and C.-h. Chen, *Nat. Mater.*, 2021, **20**, 658–664.
55 Y. Wan, W. Wei, S. Ding, L. Wu, H. Qin and X. Yuan, *Adv. Funct. Mater.*, 2024, **35**, 2414554.
56 T. He, W. Wang, F. Shi, X. Yang, X. Li, J. Wu, Y. Yin and M. Jin, *Nature*, 2021, **598**, 76–81.
57 F. Tian, S. Geng, M. Li, L. Qiu, F. Wu, L. He, J. Sheng, X. Zhou, Z. Chen, M. Luo, H. Liu, Y. Yu, W. Yang and S. Guo, *Adv. Mater.*, 2025, 2501230.
58 Z. Yang, W. Lai, B. He, J. Wang, F. Yu, Q. Liu, M. Liu, S. Zhang, W. Ding, Z. Lin and H. Huang, *Adv. Funct. Mater.*, 2023, **13**, 2300881.
59 L. Foppa, C. Copéret and A. Comas-Vives, *J. Am. Chem. Soc.*, 2016, **138**, 16655–16668.
60 L. Lin, S. Yao, R. Gao, X. Liang, Q. Yu, Y. Deng, J. Liu, M. Peng, Z. Jiang, S. Li, Y.-W. Li, X.-D. Wen, W. Zhou and D. Ma, *Nat. Nanotechnol.*, 2019, **14**, 354–361.